Supplementary Materials for

A plant-friendly wearable sensor for reducing interfacial abiotic stress effects and growth monitoring

Haoyan Xu[1,2,3], Han Wu[1,2,3], Na Jia[1,2], Yuan Bai[1,2], Liangkuan Zhu[1,2,], Chenrui Sun[1,2], Dongnan Xu[1,2], Wenlong Song[1,2,*], Zhuangzhi Sun[1,2,*]*

[1] *Province Key Laboratory of Forestry Intelligent Equipment Engineering, College of Mechanical and Electrical Engineering, Northeast Forestry University, Harbin 150000, People's Republic of China.*

[2] *Key Laboratory of Biobased Material Science & Technology, Ministry of Education, Northeast Forestry University, Harbin 150000, People's Republic of China.*

[3] *These authors contributed equally to this work.*

[*] *Corresponding authors. Email: sunzhuangzhi@nefu.edu.cn zhulk@nefu.edu.cn swl@nefu.edu.cn*

Brief description of what this file includes:

Fig. S1. Preparation process of hexagonal prism array structure.

Fig. S2. The airflow test through the ventilator of the hexagonal prism array structure.

Fig. S3. A device for simulating plant transpiration and verifying that the hexagonal array structure with an escape route for water vapor.

Fig. S4. Microstructure of the hexagonal prism array on the surface of the PW sensor.

Fig. S5. Structural optimization of hexagonal prism arrays.

Fig. S6. Reproducibility of hexagonal array structures.

Fig. S7. Mechanical properties of the PW sensor.

Fig. S8. XRD pattern of the PW sensor.

Fig. S9. Effect of a single factor (light, presence or absence of hexagonal array structure) on chlorophyll content of plant leaves.

Fig. S10. Rate of stomatal opening decline in plant leaves, leaves with PW sensors attached, and leaves with general hydrogel sensors attached.

Fig. S11. A wireless monitoring system for temperature and humidity in plant microenvironments based on the PW sensor.

Fig. S12. Performance of wireless monitoring system for temperature and humidity in plant microenvironment.

Table S1. Fluctuations in the rate of change of resistance of the PW sensor with temperature variation.

Table S2. Fluctuations in the rate of change of resistance of the PW sensor with humidity variation.

Note S1. POD and SOD quantification assays.

Note S2. Hexagon size optimization.

Note S3. Hexagonal repeatability.

Note S4. XPS and FT-IR characterization analysis of the PW sensor.

Note S5. Numerical simulation and flow field imaging analysis.

Note S6. XRD analysis of the PW sensor.

Note S7. VHX-5000 ultra-depth 3D microscope operation steps.

Note S8. Principle of wireless monitoring system for plant microenvironment temperature and humidity.

References.

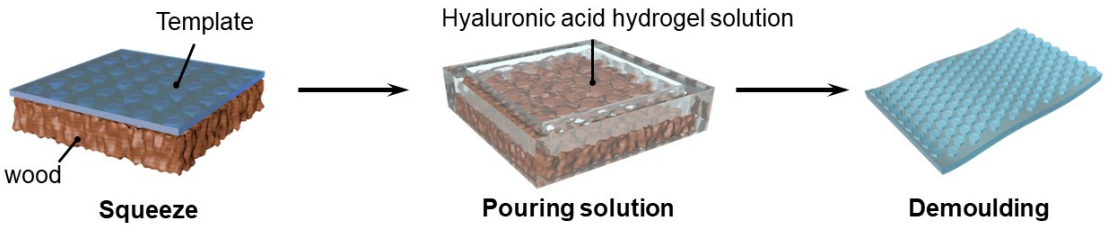

Fig. S1. Preparation process of hexagonal prism array structures on the surface of the PW sensor.

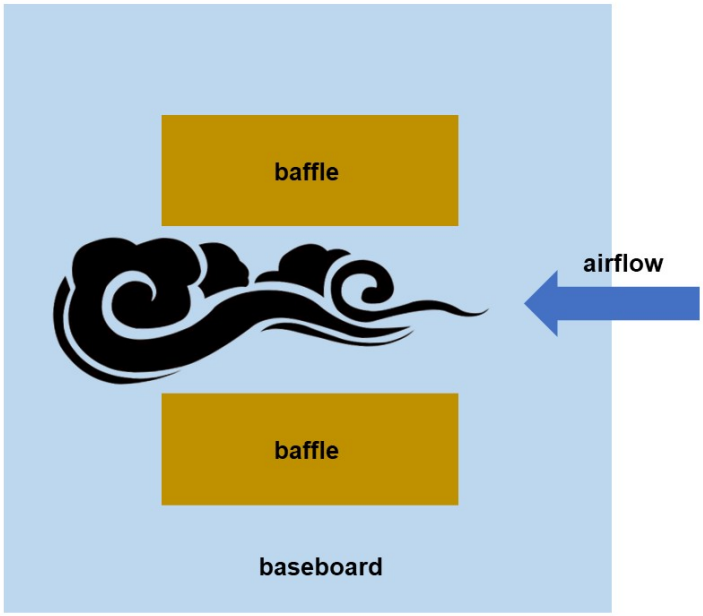

Fig. S2. The airflow test through the ventilator of the hexagonal prism array structure. The anterior and posterior sides were enclosed and a uniform airflow was passed from the left side to the right side for observing the airflow through the ventilator of the hexagonal prism array structure.

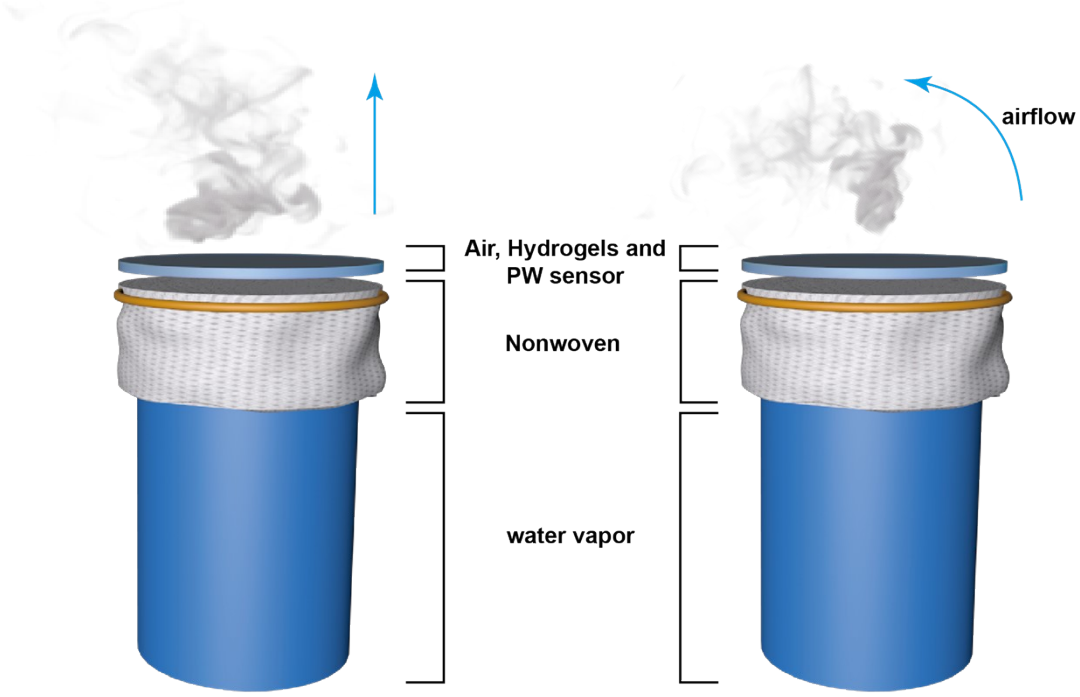

Fig. S3. A device for simulating plant transpiration and verifying that the hexagonal array structure with an escape route for water vapor.

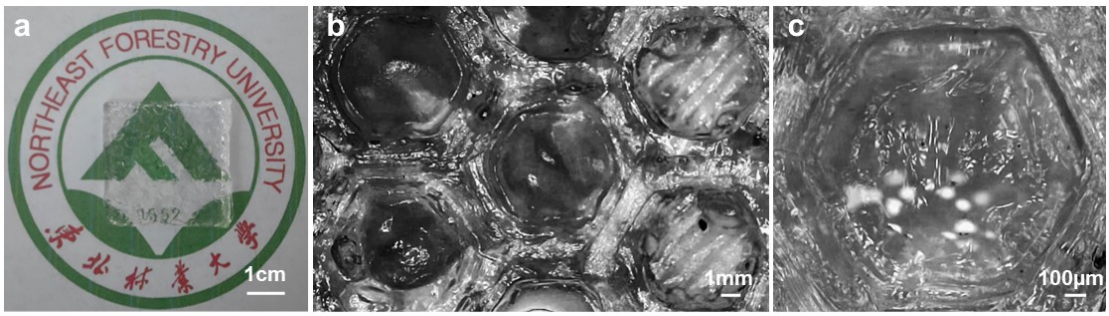

Fig. S4. Microstructure of the hexagonal prism array on the surface of the PW sensor. (a) Physical drawing of hexagonal prism array on the PW sensor surface. (b) 10× magnification of the hexagonal prism array on the surface of the PW sensor. (c) 30× magnification of the hexagonal prism array on the surface of the PW sensor.

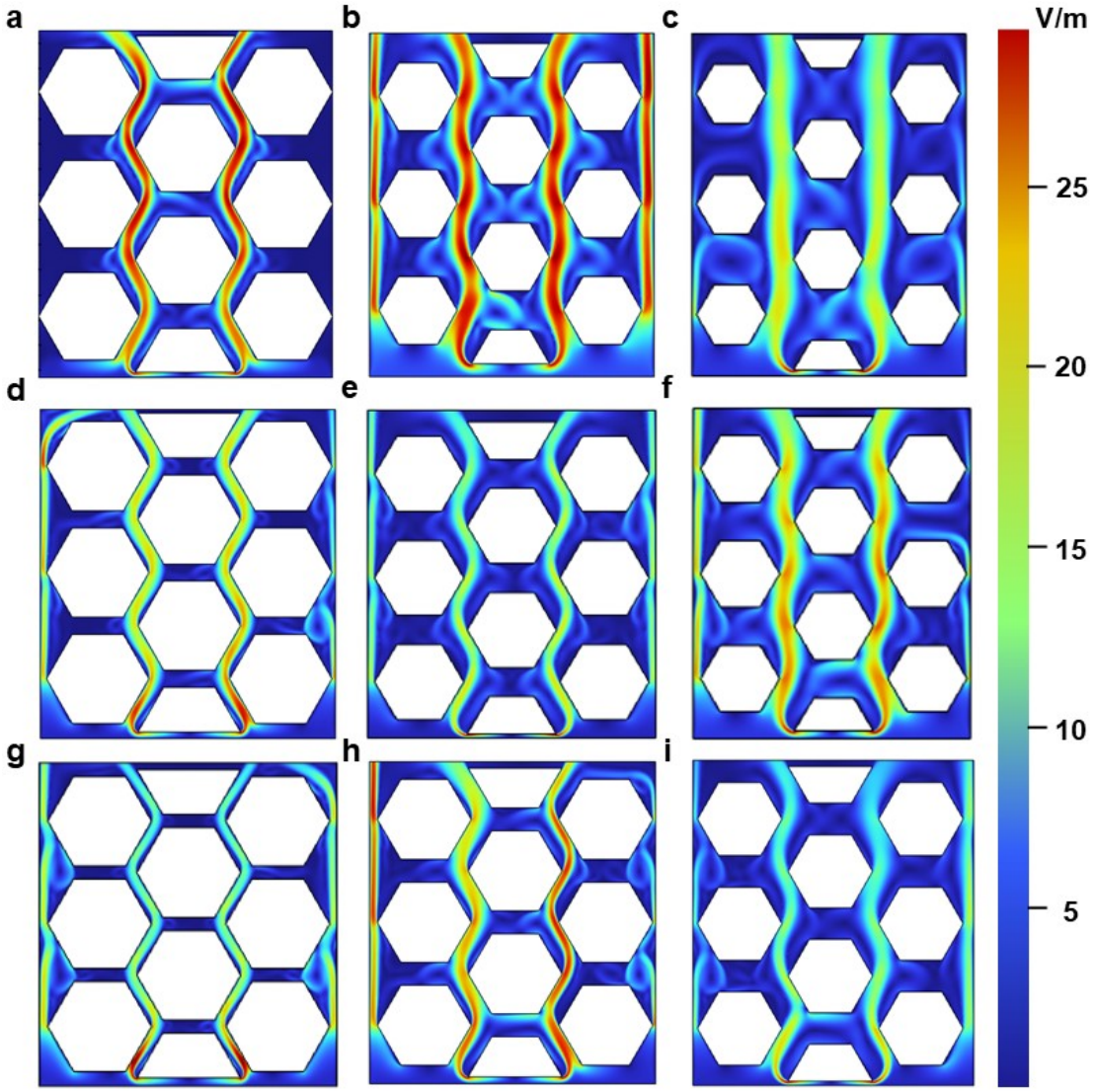

Fig. S5. Simulation optimization of hexagonal array structure. (a) Hexagonal side length (d)=2 cm, hexagonal gap (l)=0.5 cm; (b) d=2 cm, l=1 cm; (c) d=2 cm, 1.5 cm; (d) d=3 cm, l=0.5 cm; (e) d=3 cm, l=1 cm; (f) d=3 cm, l=1.5 cm; (g) d=4 cm, l=0.5 cm; (h) d=4 cm, l=1 cm; (i) d=4 cm, l=1.5 cm.

The results are shown in Fig. S5, we find that if the gap between the arrays is too small, it will not accelerate the fluid, but rather inhibit the escape of the fluid. And the gap is too big will make the channel almost straight and the acceleration effect is poor. Therefore, it can be seen from the figure that only figure (b), i.e., a surface area of 2.6 cm^{-2} and a gap of 1 cm between arrays can satisfy the rapid passage of the fluid, while all other cases have the problem of slow flow rate or low flow rate.

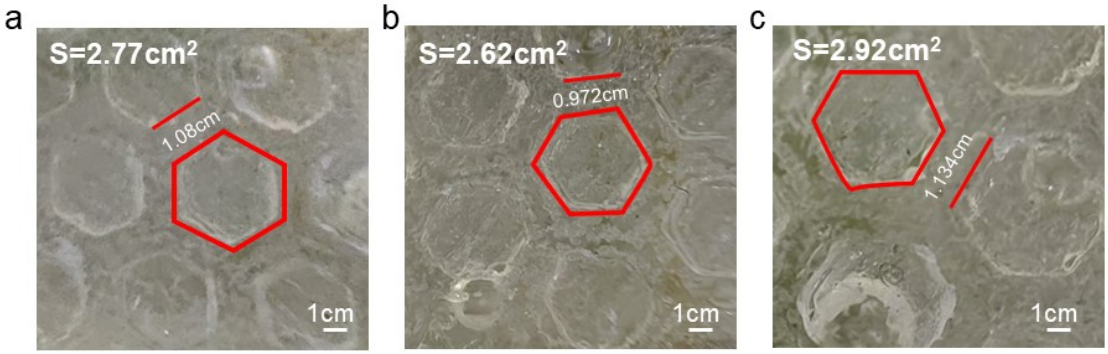

Fig. S6. Repeatability of PW sensor hexagonal prism array structures. (a)-(c) Dimensions of three sets of PW sensor hexagonal prism arrays prepared.

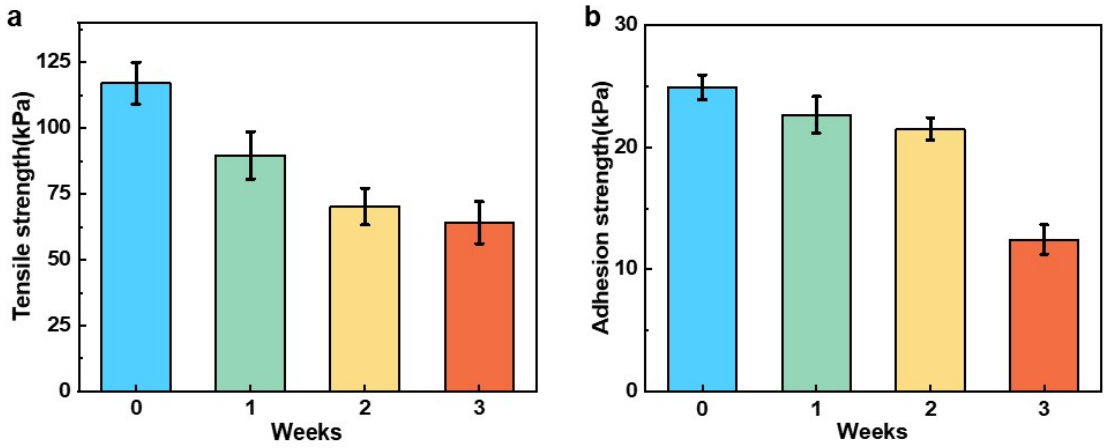

Fig. S7. Mechanical properties of the PW sensor. (a) Tensile properties of the PW sensor. (b) adhesion properties of the PW sensor.

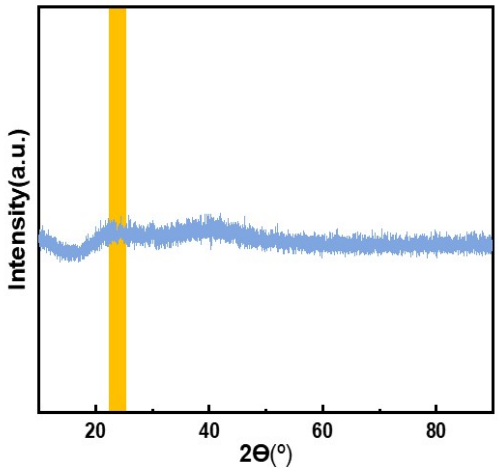

Fig. S8. XRD pattern of the PW sensor.

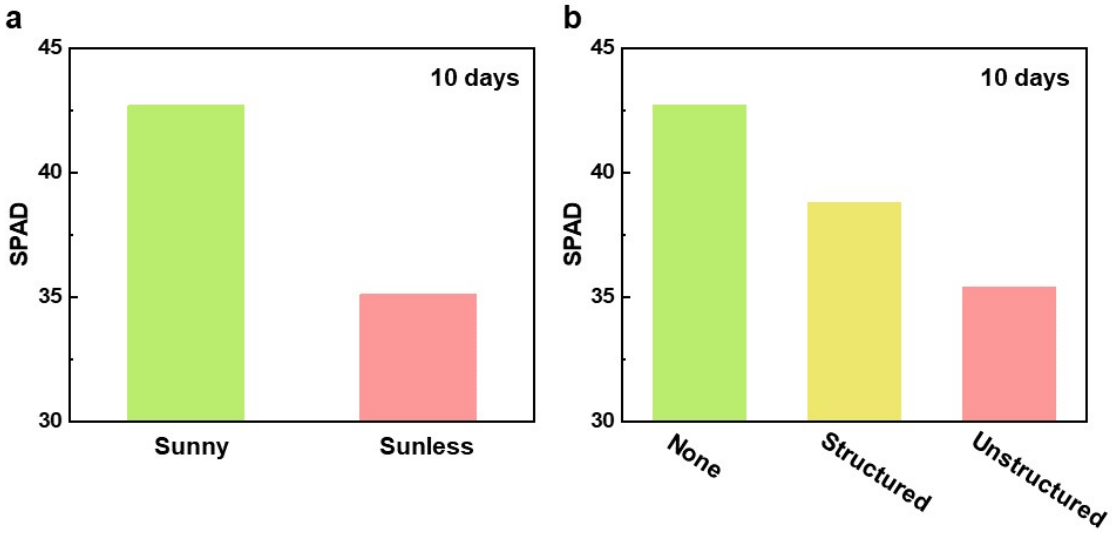

Fig. S9. Effect of a single factor (light, presence or absence of hexagonal array structure) on chlorophyll content of plant leaves. (a) Effect of light on chlorophyll content of plant leaves. (b) Effect of hexagonal array structure on chlorophyll content of plant leaves.

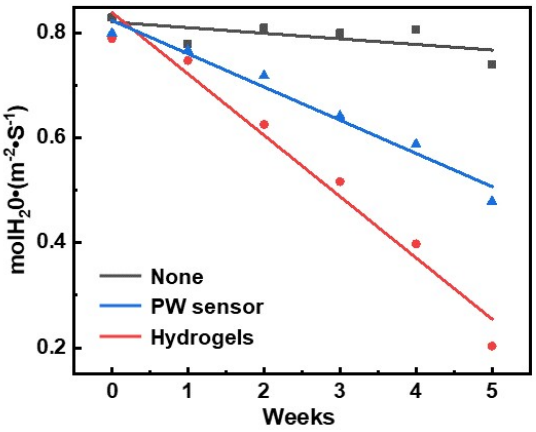

Fig. S10. Rate of stomatal opening decline in plant leaves, leaves with PW sensors attached, and leaves with general hydrogel sensors attached.

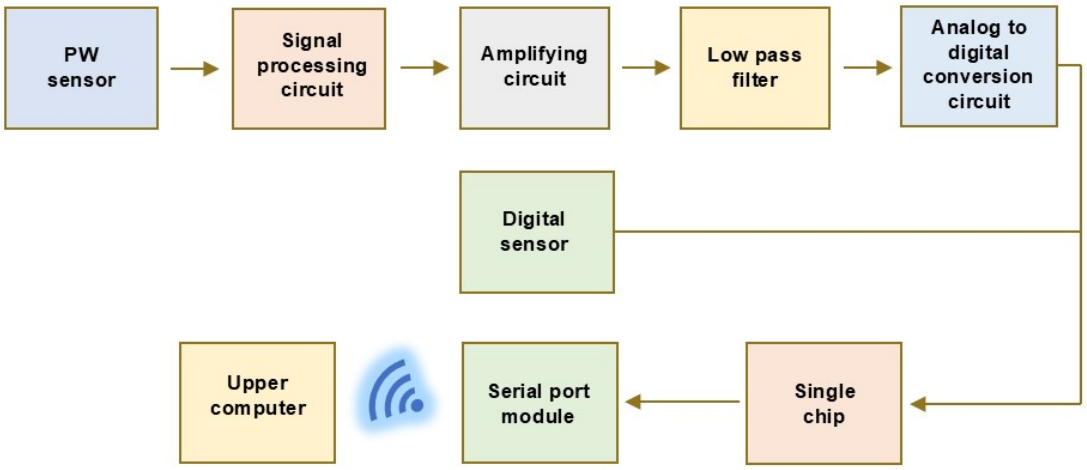

Fig. S11. A wireless monitoring system for temperature and humidity in plant microenvironments based on the PW sensor.

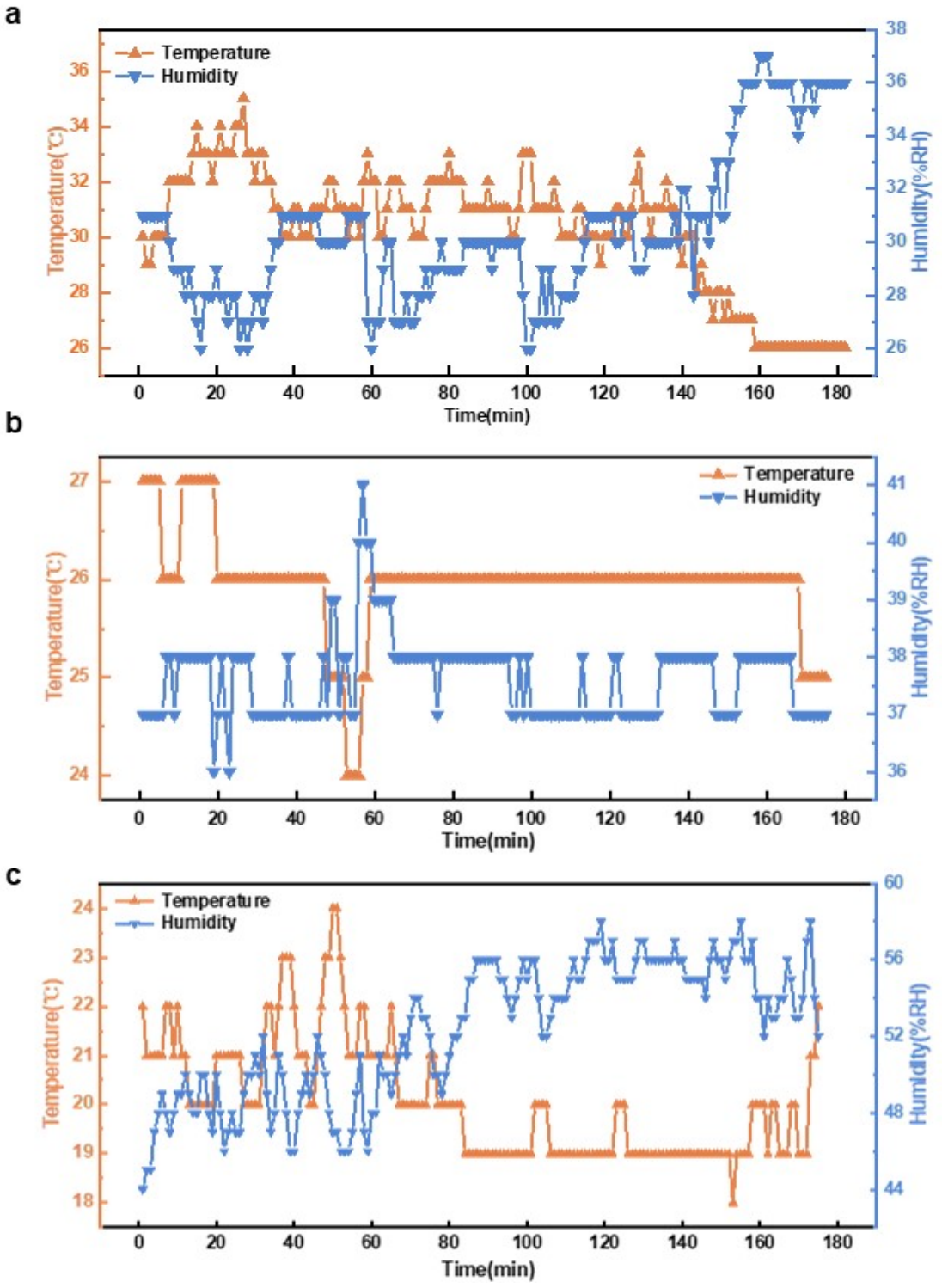

Fig. S12. Performance of wireless monitoring system for temperature and humidity in plant microenvironment. The monitoring system monitors the temperature and humidity around the leaves in the (a) morning, (b) afternoon and (c) evening.

Table S1. Fluctuations in the rate of change of resistance of the PW sensor with temperature variation.

T	Cycle							
	1	2	3	4	5	6	7	8
20 ℃	0	-0.041	0.007	-0.062	0.004	-0.019	0.122	-0.004
80 ℃	0	-0.095	-0.001	0.052	0.049	0.029	-0.014	0.046

Table S2. Fluctuations in the rate of change of resistance of the PW sensor with humidity variation.

% RH	Cycle							
	1	2	3	4	5	6	7	8
20% RH	0	0.019	0.021	0.021	0.019	0.047	0.065	0.074
80% RH	0	0.116	0.029	0.026	0.014	0.028	0.043	0.023

Note S1. POD and SOD quantification assays.

POD test: Weigh about 0.1 g of specimen, add 1 mL of extraction solution and homogenize in an ice bath. After that, the sample was centrifuged at 4 ℃×12000 rpm for 10min, and the supernatant was removed and placed on ice for measurement.

The spectrophotometer was preheated for 30 min and the wavelength was adjusted to 470 nm and zeroed with distilled water. The sample and detection reagent were added sequentially into a 1 mL glass cuvette. Immediately after mixing, the absorbance value A1 was read at 470 nm and the absorbance value A2 was read after 1 minute.

Calculation of POD enzyme activity: The enzyme activity was calculated on the basis of the fresh weight of the sample and was defined as one unit of enzyme activity, U, per gram of tissue per minute of increase in absorbance at 470 nm by 0.5 per minute in the reaction system.

$$\mathrm{POD}(\Delta\mathrm{OD}/\mathrm{min}/\mathrm{g}) = (\mathrm{A}_2 - \mathrm{A}_1) \div (\mathrm{W} \times \mathrm{V}_1 \div \mathrm{V}) \div 0.5 \div \mathrm{T}$$

V is the volume of extract added; V_1 is the volume of sample added; T is the reaction time; W is the sample mass.

SOD test: Take 0.1 g of tissue, add 1 mL of extraction solution, and then centrifuge at 4 ℃×12000 rpm for 10min. take the supernatant as the test solution.

The spectrophotometer was preheated for 30 min and the wavelength was adjusted to 450 nm and zeroed with distilled water. The test reagent was placed in a water bath at 25 °C for more than 5 min. Then the detection reagent and sample were added sequentially in a 1mL glass cuvette. After sufficient mixing, the absorbance value A of each tube was measured at 450 nm after standing for 30 min at room temperature (25 ℃) away from light.

SOD enzyme activity calculation:

1. Calculation of percentage inhibition:

$$\text{Percentage inhibition} = \left[\left(\mathrm{A}_{\text{blank tube 1}} - \mathrm{A}_{\text{blank tube 2}}\right) - \left(\mathrm{A}_{\text{specimen tube}} - \mathrm{A}_{\text{specimen control tube}}\right) \right] / \left(\mathrm{A}_{\text{blank tube 1}} - \mathrm{A}_{\text{blank tube 2}}\right) \times 100\%$$

2. SOD enzyme activity unit: At 50% inhibition in the above xanthine oxidase coupled reaction system, the SOD enzyme activity in the reaction system is defined as one enzyme activity unit.

(Calculated on the basis of the fresh weight of the sample):

$$\mathrm{SOD}(\mathrm{U}/\mathrm{g}) = \left[\text{Percentage inhibition} \div \left(1 - \text{Percentage inhibition}\right) \times \mathrm{V}_2 \right] \div \left(\mathrm{W} \times \mathrm{V}_1 \div \mathrm{V}\right) \times \mathrm{D}$$

V is the volume of extract added; V_1 is the volume of sample added to the reaction system; V_2 is the total volume of the reaction system; D is the sample dilution; W is the sample mass.

Note S2. Hexagon size optimization.

We investigated the effect on the air flow etc. by varying the surface area of individual hexagonal faces in the hexagonal prism arrays and the size of the gaps between the arrays. The surface areas are 2.6 cm^2, 5.85 cm^2 and 10.39 cm^2, and the gaps between the arrays are 0.5 cm, 1 cm and 1.5 cm, respectively. The results are shown in Fig. S5. We find that if the gap between the arrays is too small, it will not accelerate the fluid, but rather inhibit the escape of the fluid. And the gap is too big will make the channel almost straight and the acceleration effect is poor. Therefore, it can be seen from the Fig. S5(b), i.e., a surface area of 2.6 cm^2 and a gap of 1 cm between arrays can satisfy the rapid passage of the fluid, while all other cases have the problem of slow flow rate or low flow rate.

Note S3. Hexagonal repeatability.

We tested the repeatability of the hexagonal prism array. We selected a mold with a hexagonal area of 2.6 cm^2 and a gap of 1 cm, and prepared three sets of PW sensors. The results are shown in Fig. S6. The prepared structures exhibit a high degree of repeatability, indicating the reliability and consistency of the preparation process. The three groups have only 0.7%-10.9% error in the area and 2.8%-13.4% error range in the gap, which is very small difference from the mold, indicating the high stability of the process.

Note S4. XPS and FT-IR characterization analysis of the PW sensor.

X-ray photoelectron spectroscopy (XPS) and Fourier transform infrared spectroscopy (FT-IR) analyses confirmed the internal chemical structure and cross-linking of the PW sensor. As shown in Fig. 1c, due to the hydrogen bond formation between AA~co~AM and HA, the stretching vibration of the carbonyl group was shifted to 1706 cm-1 compared to pure HA. The peaks at 3331 cm^{-1} and 1162 cm^{-1} can be attributed to the O-H stretching of the HA and the PW sensor, the N-H stretching and -C=O stretching. The N-H stretching band of the PW sensor at 3347 cm^{-1} is higher than that of the AM at 3331 cm^{-1}. The O-H absorption moves to around 3331 cm^{-1}. Due to the formation of hydrogen bonding between the PW sensor and HA, the stretching vibration of the carbonyl group in the PW sensor moved to 1670 cm^{-1} at 1634 cm^{-1} compared to pure HA[1-4]. In Fig. 1d, the XPS C 1s spectrum shows signals of three major components: carbonyl (287.99 eV), C-O/C-N (286.27 eV), and C-C/C-H (284.8 eV). Among them, the characteristic C-O/C-N peaks are very obvious because of the presence of a large number of C-O in the glycerol molecule, which interact with other molecules in the hydrogel network through hydrogen or covalent bonds, which confirms the successful introduction of glycerol. These results indicate the successful synthesis of the PW sensor.

Note S5. Numerical simulation and flow field imaging analysis.

Fig. 2b illustrates the distribution of air flow velocity in the hexagonal prism array structure. According to aerodynamic principles, the air flow velocity accelerates significantly as it enters the narrow channel from the spacious area. The color gradient in Fig. 2b shows the change in air flow velocity, as air enters the hexagonal prism array structure, the narrow portion of the channel significantly accelerates the air flow, resulting in a much higher velocity. This acceleration effect is critical for the rapid expulsion of water vapor and other substances, as it reduces the retention of water vapor between the sensor and the plant, thereby mitigating the negative impact on the plant microenvironment. The hexagonal array structure not only optimizes air flow, but also enhances the efficiency of gas exchange between the sensor and the plant, helping to maintain normal physiological functions of the plant.

Fig. 2c shows the effect of two different sensor designs (Fig. 2c i, Fig. 2c ii) on air flow by comparison. Fig. 2c i demonstrates that under the hexagonal prism array structure, the air flow is pressed inward and into the low-velocity, high-pressure environment after exiting the high-velocity, low-pressure hexagonal array structure. This design effectively directs the air flow so that it can pass smoothly over the sensor surface, thereby helping to expel water vapor and other substances and reducing the environmental stress on the plant.

In contrast, Fig. 2c ii demonstrates the effect of a conventional hydrogel sensor. In contrast to the hexagonal array structure, the conventional hydrogel sensor almost completely closes off the air flow pathway, preventing the expulsion of water vapor and other substances. This design lacks aerodynamic optimization, resulting in water vapor being trapped between the sensor and the plant, which increases abiotic stresses on the plant, such as increased humidity.

Note S6. XRD analysis of the PW sensor.

The X-ray diffraction pattern of the PW sensor shows a broad diffraction peak centered at $2\theta \approx 22°$, which indicates the presence of an amorphous structure of the PW sensor.

Note S7. VHX-5000 ultra-depth 3D microscope operation steps.

First, a suitable base plate should be selected, and the specimen should be placed on it. A suitable lens magnification is then selected, and the brightness and focus are adjusted. The opening and closing of the stomata can then be observed in real time, and photos can be taken.

Note S8. Principle of wireless monitoring system for plant microenvironment temperature and humidity.

As shown in Fig. S11, we built a flexible temperature/humidity sensor measurement system to realize the process of obtaining temperature and humidity data from PW sensors for. The hardware part of the system designed in this paper mainly includes STM32F405RGT6 chip, A/D conversion, serial communication, signal conditioning circuit, amplification circuit, low-pass filtering and Bluetooth transmission and other modules. The microcontroller selected for the flexible temperature and humidity sensor measurement system is STM32F405RGT6 of STM32 series, which serves the following purposes: to collect the temperature and humidity data from the flexible temperature/humidity sensor. The system software part is mainly completed by LabVIEW. According to the overall requirements of the hardware design of the system, the required chip modules are integrated into the PCB experimental board. Test and debug the experimental board to ensure that the function is normal, and then access the flexible temperature and humidity sensor. Through VISA, realize the communication between the lower computer and the upper computer LabVIEW. At the same time by reading bytes, complete the temperature and humidity display on the host computer.

References

1 S. Wu, C. Gong, Z. Wang, S. Xu, W. Feng, Z. Qiu and Y. Yan, *Adv. Sci.*, 2023, **10**.

2 R. Liu, Y. Liu, Y. Cheng, H. Liu, S. Fu, K. Jin, D. Li, Z. Fu, Y. Han, Y. Wang and Y. Tian, *Adv. Funct. Mater*, 2023, **33**.

3 H. Zhu, T. Yang, S. Chen, X. Wang, J. He and Y. Luo, *Adv. Compos. Hybrid Mater.*, 2023, **6**.

4 X. Dang, Y. Fu and X. Wang, *Biosens. Bioelectron*, 2024, **246**.